JOURNAL OF GEOPHYSICAL RESEARCH, VOL. 100, NO. A4, PAGES 5819–5825, APRIL 1, 1995

$O(^1S)$ 557.7 nm and $O(^1D)$ 630 nm emissions in shuttle thruster plumes

R. A. Viereck,[1] E. Murad,[1] C. P. Pike,[1] S. B. Mende,[2] G. A. Swenson,[2]
J. B. Elgin,[3] L. S. Bernstein,[3] and S. Lucid[4]

Abstract. Radiation resulting from interaction between the effluent cloud of a space shuttle thruster and the ambient atmosphere was observed with a spectrograph aboard the shuttle. The spectral measurements were made between 400 and 800 nm with a resolution of 3 nm. The primary emissions are identified as NO_2, HNO, $O(^1D)$, and $O(^1S)$. These are the first observations of $O(^1S)$ emission in the shuttle plume. These data are compared with previous measurements, and possible excitation mechanisms are discussed. The results are also compared with a Monte Carlo simulation of thruster plume-atmosphere interaction radiation.

Introduction

In low Earth orbit the composition and density of local atmospheres of spacecraft, in general, and of the space shuttle, in particular, are different from the ambient atmosphere. This observation is documented particularly well for the space shuttle because of its ready accessibility for experiments. For example, the complex nature of the local atmosphere of the space shuttle is strongly affected by the firings of the attitude control thrusters (see, for example, *Scialdone* [1986], *Carignan and Miller* [1987], *Ehlers* [1986], *Pickett et al.* [1985], and *Wulf and von Zahn* [1986]). Supplementing these composition studies are measurements of the optical environment that have until now concentrated mostly on the space shuttle glow phenomenon (see *Viereck et al.* [1992] for a recent discussion). Ground observations of optical emissions generated by the interaction of thruster effluents with the atmosphere [*Broadfoot et al.*, 1992] show the presence of both NH emissions at 337 nm and $O(^1D)$ emissions at 630 nm, the latter being generated primarily by excitation of ambient atmospheric $O(^3P)$ in collisions with engine exhaust. The $O(^1D)$ emission was observed to extend several kilometers from the point of origin; however, the $O(^1S)$ emission was not observed at all. In that study, it was speculated that emission from $O(^1S)$ should have been observed if the estimated rate coefficients were correct.

Optical emissions around spacecraft such as the shuttle could adversely affect optical measurements from space, especially since the $O(^1S)$ and $O(^1D)$ emissions are the primary emissions in the nightglow and aurora. The space shuttle represents a generic large space platform from which a study of these emissions is possible (similar effects would be expected in using the space station). We have therefore examined thruster plume emissions from the $O(^1D) \rightarrow O(^3P)$ transition at 630 nm and the $O(^1S) \rightarrow O(^1D)$ transition at 557.7 nm using a handheld spectrograph, part of the Auroral Photography Experiment (APE). This experiment was used recently to identify NO_2 emissions in terrestrial nightglow [*Mende et al.*, 1993] and to identify HNO and NO_2 emissions near the nozzle of the thrusters [*Viereck et al.*, 1991, 1993]. We present here the first observations of the $O(^1S)$ emission 557.7 nm generated by the interaction of the space shuttle engine exhaust gases with the ambient atmosphere.

Instrumentation and Analysis

The APE spectrograph consisted of three standard camera lenses, 50 and 55 mm focal lengths, and a slit and diffraction grating to disperse the light. The dispersed light was focused onto an image intensifier with a 25-mm S-20 photocathode, and the phosphor output screen of the intensifier was refocused optically onto 35-mm film. The spectral range of the APE spectrograph was from 380 to 800 nm with a spectral resolution of about 4 nm, if all of the optical focuses are optimized. The instrument was mounted in the crew cabin of the space shuttle such that images and spectra of the tail region of the shuttle could be recorded through the aft flight deck window. A detailed description of the instrument was presented by *Viereck et al.* [1992].

The instrument was used in two configurations. The first configuration was the imaging mode where the slit and grating were removed from the optical path to produce an image of the target on the photocathode. In this mode, the slit was replaced by a mask to show the location of the slit in the target image. The second configuration was the spectrograph mode where the slit and grating were placed into the optical path to disperse the light from the target in wavelength. In this mode, one dimension of spatial information was recorded as fluctuations in brightness parallel to the spectrograph slit.

Figure 1 shows an image taken with the APE spectrograph in the imaging mode. In Figure 1, the placement and alignment of the slit in reference to the tail region of the shuttle is shown by the dark vertical band. Once the instrument was aligned, the slit and grating were inserted into the optical path, and a series of spectra were taken while an aft thruster was fired. Figure 2 shows two 4-s exposures taken in the

[1]Phillips Laboratory, Spacecraft Interactions Branch, Hanscom Air Force Base, Massachusetts.
[2]Lockheed Research Division, Palo Alto, California.
[3]Spectral Sciences Incorporated, Woburn, Massachusetts.
[4]NASA Johnson Space Center, Houston, Texas.

Paper number 94JA03371.
0148-0227/95/94JA-03371$05.00

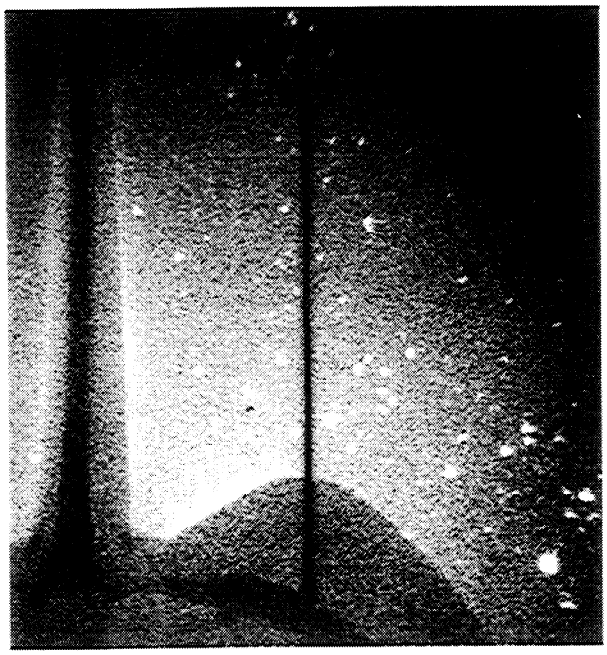

Figure 1. An image of the tail region of the space shuttle taken with the Auroral Photography Experiment (APE) instrument in the imaging mode. The black stripe running vertically through the image indicates the position and alignment of the spectrographic slit.

spectrograph mode during and immediately after a 4-s thruster firing. The light is dispersed spectrally along the horizontal axis, but spatial information is retained is retained in the vertical direction (parallel to the spectrograph slit).

The shuttle was placed into a backward attitude so that the tail was pointed into the ram direction and the shuttle bay was directed away from the Earth. The thruster that was observed was an aft-firing thruster and therefore fired directly into the oncoming atmosphere. The experiment was performed in August 1991 at 325 km altitude over the Indian Ocean (2°S, 90°W) on the shuttle flight STS 43. The Sun and new Moon were at 178° zenith angle, so scattered sunlight did not contribute to the observed radiances. A similar experiment was performed in March 1994. The shuttle attitude was such that the plume and observations were perpendicular to the velocity vector, and the shuttle altitude was 209 km. A comparison of these observations will be given.

The shuttle engine was part of the primary reaction control system (PRCS). Each PRCS engine has a thrust of 870 lbs (196 N) and a mass flow of 1420 g/s. The exhaust of these engines consists primarily of N_2 (~40 mol%), H_2O (~30%), CO (~15%), and CO_2 (~10%) [*Trinks and Hoffman*, 1984]. The gas exit velocity is ≈ 2.9 km/s, and it rapidly increases to 3.5 km/s because of the expansion of the plume exhaust into the near-vacuum of space. For a ram-fired engine, the total plume-atmosphere molecular collision velocity is given by the sum of the vacuum-expanded exhaust velocity and the vehicle orbital velocity. In this experiment, the collision velocity is ≈ 11.3 km/s resulting in a center-of-mass collision energy (the precise value depends on the collision partners) in excess of 5 eV. The collision velocity and energy for a perpendicular-fired engine is about 8 km/s and 3.5 eV, respectively.

Figure 3 shows how the line of sight of the spectrograph intersects the plume of the thruster. The spectrograph was pointed nearly parallel with the centerline of the thruster. It should be noted that the thruster is pointed 10° up from the horizontal axis of the shuttle. Thus the centerline of the plume appears above the shadow line of the orbital maneuvering system (OMS) pod several meters from the plume nozzle. If viewed from above, the centerline of the PRCS thruster also crosses the center of the APE field of view several meters from the nozzle.

The two spectral images shown in Figure 2 were each taken with a 4-s exposure time. The spectrographic images are dispersed in wavelength along the x axis, distance (or angle) along the y axis, and relative brightness represented by gray shades along the z axis. The first spectrographic image was taken concurrently with the thruster firing. There is a continuum across much of the spectrum and two line emissions at 557 and 630 nm. The OMS pod shadow is seen as a sharp edge of the bright region in the spectral image.

The second spectral image (Figure 2b) was taken immediately after the thruster firing and shows no continuum but does show a faint line at 630 nm. In this frame, the spectral line does not exhibit the sharp cutoff at the lower boundary as is observed in Figure 2a. Instead, the line extends below

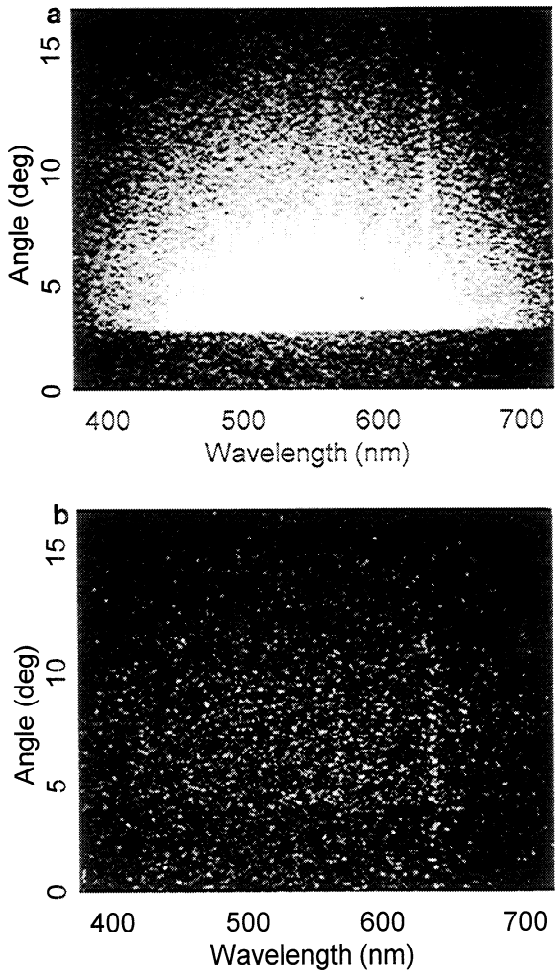

Figure 2. Spectral images of the primary reaction control system (PRCS) thruster plume. (a) A 4-s exposure taken simultaneously with the 4-s thruster firing. (b) A 4-s exposure taken immediately after the engine firing.

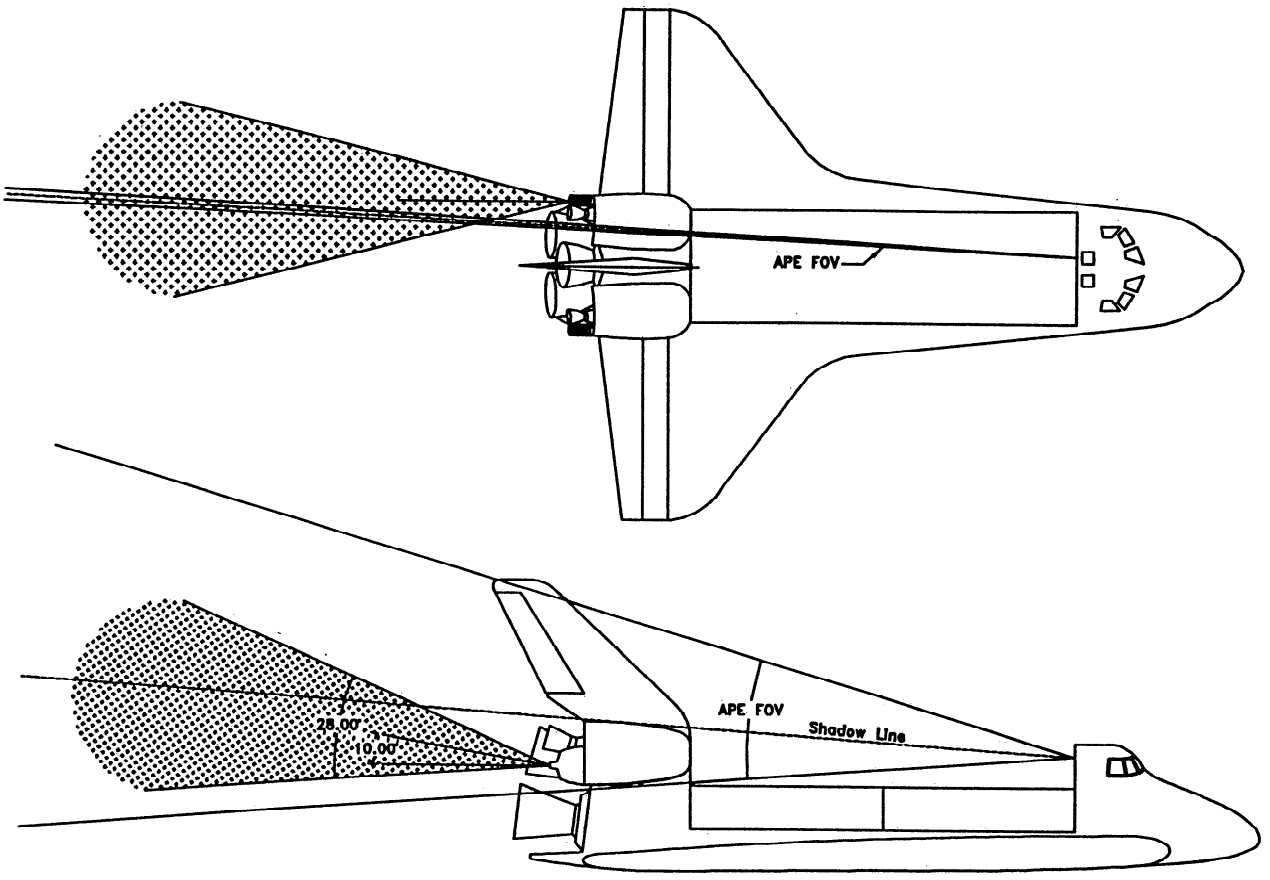

Figure 3. The alignment of the APE spectrograph. The slit was oriented vertically so that the spatial information was in the vertical direction. Note that the PRCS engine is canted up 10° from the centerline of the shuttle.

the shadow line of the OMS pod. The implications of this will be presented in the discussion section. It should be noted that these spectrographic images are two of a series of five taken during this test. The spectrum taken before and the three spectra taken after the two shown here have no spectral features, indicating that there were no measurable emissions before or after the engine burn. A repeat of this sequence of exposures showed the same results.

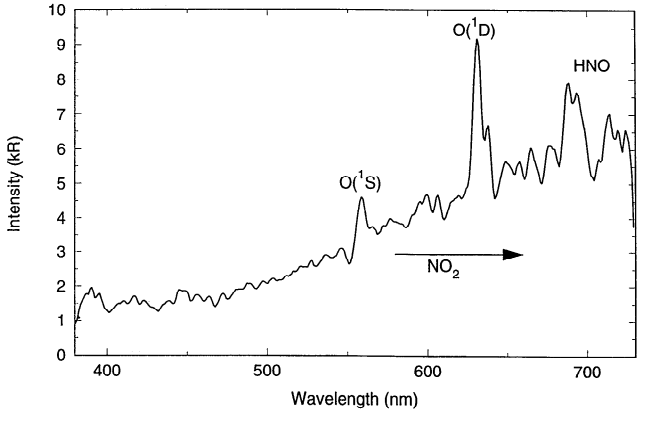

Figure 4. The rows in Figure 2a were co-added to form a spectrum. The spatial integration was done over the 5 deg of the field of view closest to the OMS pod shadow line. Four of the most dominant emission features are labeled.

The spectrographic images were digitized, and rows of pixels were co-added to produce a line spectrum of the plume emissions. Before and after the experiment the instrument was exposed to the nighttime terrestrial limb, and the resulting nightglow emissions were used to calibrate the wavelength scale and to check the radiance calibration. The data in Figure 2a were processed and calibrated for relative sensitivity, and the resulting intensity of the 557.7-nm emission is of the order 1.5–2 kR (1 kR = 10^9 photons cm^{-2} s^{-1}). The spectrum shown in Figure 4 was summed across 5° of the field of view starting just at the shadow of the OMS pod. The data shown in Figures 2 and 4 are from the shuttle mission STS 43 taken in August 1991. Similar data were collected on STS 62 in March 1994. On this mission, the instrument and viewing geometry were the same except that the shuttle was placed in a wing-to-ram attitude so that the thruster fired perpendicular to the ram direction. Another difference between the data taken on STS 43 and STS 62 was the altitude which was 325 and 209 km, respectively. Once again both the $O(^1D_2)$ and $O(^1S_2)$ emissions were observed in the plume. In our analysis we will compare the ratios of the two emissions since absolute comparisons are made difficult because of the large difference in altitude and the instrument variability from mission to mission.

Table 1. Preexponential Rate Constants for (^1S) Quenching

Reaction	Quenching Rate
$O(^1S) + H_2O \rightarrow O(^3P) + H_2O$	5.4×10^{-11a}
$O(^1S) + CO_2 \rightarrow O(^3P) + CO_2$	$1.2 \times 10^{-11a,b}$
$O(^1S) + CO \rightarrow$ Products	7.4×10^{14b}
$O(^1S) + H_2 \rightarrow$ Products	2.9×10^{-16b}
$O(^1S) + N_2 \rightarrow$ Products	$\leq 5 \times 10^{-17c}$

Units of cm^3 molecules^{-1} s^{-1}.
[a]From *Slanger and Black* [1978].
[b]From *Capetanakis et al.* [1993].
[c]From *Schofield* [1978].

Discussion

The spectral features in Figure 4 have been identified and labeled. The emission features at 557.7 and 630.0 nm are due to atomic oxygen. The line at 630.0 nm is a doublet (630.0 and 636.4 nm) which results from the transitions $O(^1D_2) \rightarrow O(^3P_{2,1})$, respectively, and is resolved in Figure 4. The $O(^1D)$ emission was reported in ground observations of the optical environment of the space shuttle [*Broadfoot et al.*, 1992]. The spectral line at 557.7 nm is due to the transition $O(^1S_0) \rightarrow O(^1D_2)$ and has not been previously identified in shuttle or rocket plumes. Note that the integrated intensity of the $O(^1D)$ emission at 630 nm is about 3 times brighter than that of the $O(^1S)$ emission at 557.7 nm. Another component of the transition from the (^1D) state (i.e., $O(^1D_2) \rightarrow O(^3P_0)$) at 639.2 nm is not normally seen because of its extremely low Einstein coefficient (cf. a full discussion by *Bates* [1982]). Other features worth noting are the NO_2 continuum in the region 400–800 nm and the banded HNO structure in the 650–720 nm region. These features have been identified in plume spectra before [*Viereck et al.*, 1993] and were attributed to the recombination of NO with O and H respectively.

We now turn to the processes by which $O(^1S)$ is formed. It is unlikely that the formation of $O(^1S)$ and $O(^1D)$ in the shuttle plumes is similar to the atmospheric process. In the upper atmosphere, $O(^1S)$ in the airglow is produced at around 100 km by the two-step Barth mechanism [*Bates*, 1982]:

$$O(^3P) + O(^3P) + M \rightarrow O_2^* + M \quad (1)$$

where O_2^* may be in the $c\,^1\Sigma_u$, $C^3\Delta$, or $A^3\Sigma_u$ states followed by a collisional exchange in energy:

$$O_2^* + O(^3P) \rightarrow O_2\left(X^3\Sigma\right) + O(^1S) \quad (2)$$

In consideration of process (1) alone, the rate coefficient frequently referenced is that of *Campbell and Gray* [1973] which is $4.7 \times 10^{-33}\,(300/T)^2$. The rate of production of O_2^* from (1) would be proportional to $[O]^2[M]$. Even with a conservative estimate of the densities this process would result in only a fraction of a Rayleigh of 557.7-nm emission. Another process prevalent in the ionosphere is recombination of O_2^+ and an electron:

$$O_2^+ + e \rightarrow O(^1D,\ ^1S) + O \quad (3)$$

which also produces a major part of the nightglow $O(^1D)$ emission. Again, it is unlikely that this process is prevalent in the plume since O_2^+ is not a major plume species nor is there evidence of electrons in significant numbers in the plume.

We look instead to collision of plume products, N_2, H_2O, CO, CO_2, and H_2, with atmospheric O for a source of the emissions. Data on the high-velocity collisional excitation of atmospheric $O(^3P)$ by the major plume species to produce $O(^1S)$ are nonexistent. An educated guess as to the most efficient plume collisional partners can be gained through consideration of the relative efficiency of the quenching of $O(^1S)$ by the plume species. It is expected that the most efficient excitation partners will also be the most efficient quenching partners. The quenching pathways of importance are the nonreactive channels that lead to ground electronic state species. The preexponential quenching rate factors of $O(^1S)$ by the major plume species are summarized in Table 1. For the quenching reactions with a measured temperature dependence (all the species but H_2O), the preexponential was chosen because it represents a "high-temperature" limit (high compared to room temperature but not in the velocity regime of the flight experiment). For CO, H_2, and N_2 the relative branching ratios into the $O(^3P)$ channel are not known, and the total quenching rates in Table 1 represent upper limits. The quenching rate constants for CO, H_2, and N_2 are 3 or more orders of magnitude below that for H_2O and indicate that these species are probably not significant collision partners even at high collision velocity. N_2 in particular represents a large mole fraction of the plume product and carries more than enough collision energy for the reaction. In addition, the quenching rate for N_2 production of $O(^1D)$ is the same as for H_2O. For these reasons, *Broadfoot et al.* [1992] concluded that $N_2 + O(^3P)$ is the dominant production mechanism for the $O(^1D)$ state. By comparison the quenching rates of $O(^1S) + N_2$ and $O(^1S) + H_2O$ differ by more than 6 orders of magnitude, and it is on this fact that we base our conclusion that the N_2 path is not important in exciting $O(^1S)$. Another possible collision partner might be CO_2. The quenching rate constant for $O(^1S) + CO_2$ is more comparable to that of $O(^1S) + H_2O$ (being smaller by a factor of 0.22). However, taking into consideration that the CO_2 mole fraction is down by a factor of 0.5 from the H_2O mole fraction indicates that the overall importance of CO_2 as a collisional excitation partner is down by about an order of magnitude relative to H_2O. Therefore, in this analysis it is assumed that the dominant excitation channel for production of $O(^1S)$ is from high-velocity collisions of atmospheric $O(^3P)$ with plume H_2O.

Energetics of $O(^1S)$ Formation

Figure 5 shows the energy required for the excitation of $O(^1S)$ and $O(^1D)$ by collisions between $O(^3P)$ and the plume species H_2O and N_2. The horizontal dashed lines at 4.19 and 1.97 eV denote the energy levels of the $O(^1S)$ and $O(^1D)$ states, respectively [*Radzig and Smirnov*, 1985]. The vertical dashed lines at 8.5 and 11.3 km/s denote the relative collision velocity of atmospheric O with plume molecules along the plume centerline for the perpendicular and ram firings, respectively. Because of the large expansion angle of the plume, there is a large spread in plume-atmosphere collision velocities. For the perpendicular firing, this spread is given by ±2 km/s about the centerline velocity. As previously discussed [*Broadfoot et al.*, 1992], both $O(^3P)$-N_2 and $O(^3P)$-H_2O collisions are important in the

excitation of the $O(^1D)$. As indicated in Figure 5, there is more than sufficient energy available to excite the $O(^1D)$ state for both the perpendicular and ram firings. This is consistent with the observations of [*Broadfoot et al.*, 1992] in which they observed $O(^1D)$ in the ram and perpendicular plumes but not in the plumes fired into the antiram direction. Figure 5 shows that from the energetics standpoint the $O(^1S)$ state is energetically accessible through $O(^3P)$ + H_2O collisions [*Slanger and Black*, 1978], and there is sufficient excitation energy in the ram firings. The perpendicular plumes would be very close to the energy threshold for the production of $O(^1S)$ if it were not for the velocity spread resulting from thermal motion and plume expansion in the nozzle. It should also be noted that there is sufficient energy for the $O(^1S)$ state to be formed by the $O(^3P)$ + N_2 reaction as well, but the quenching rate argument presented in the previous section makes this reaction unlikely as a source of the emission.

Observing the ram angle dependence of the 557.7- and 630-nm emission might provide some insight into the question of whether N_2 or H_2O is the dominant collision partner. Our observations show that there is indeed $O(^1S)$ in the plume as indicated by the 557.7-nm emission in our data. The energy argument implies that the brightness of the 557.7-nm emission should fall off faster with ram angle than the 630-nm emission. The available center of mass energies show that, if all other things were equal, 557.7-nm emission for the H_2O reaction would decrease faster with increasing ram angle than for the N_2 reaction simply because of the higher mass of N_2. Our data show that the ratio of the integrated intensities of 630–557.7 nm is about 3:1 for the ram burn at 325 km altitude and 7.5:1 for the perpendicular burn at 209 km altitude. It is difficult to compare brightnesses of the data due to numerous variables, but qualitatively, the perpendicular burn at lower altitude is 2–4 times brighter than the ram burn at higher altitudes.

SOCRATES Calculations

If we assume that H_2O is the primary reactant species, we can examine detailed phenomenology of $O(^1S)$ using the Shuttle Orbiter Contamination Representation Accounting for Transiently Emitted Species (SOCRATES) code [*Elgin et al.*, 1990]. With the aid of the calculations we can explain the temporal and spatial nature of the observations and infer state-specific rate constants for the excitation of $O(^1S)$ by collisions with H_2O.

It can be seen in Figure 4 that the space observations reveal that the brightness of the $O(^1S)$ emission is approximately $\frac{1}{4}$ the brightness of the $O(^1D)$ emission. The O-H_2O excitation rate constant for $O(^1S)$ production was adjusted until good agreement with the experimental data was obtained. The final value was found to be 1.35×10^{-12} cm^{-3} mol^{-1} s^{-1} which represents a rough approximation based on the data. It should be noted that this value is 40 times smaller than the quenching rate of the $O(^1S)$ + H_2O reaction as reported by *Slanger and Black* [1978]. This is reasonable since the temperatures are vastly different with the quenching rate determined at room temperature, and the reaction rate calculated here is for temperatures of 2000°–3000°K.

Dynamics of $O(^1S)$ Formation

In addition to the total intensity of the $O(^1S)$ emission discussed above, the shape of the emission region can yield

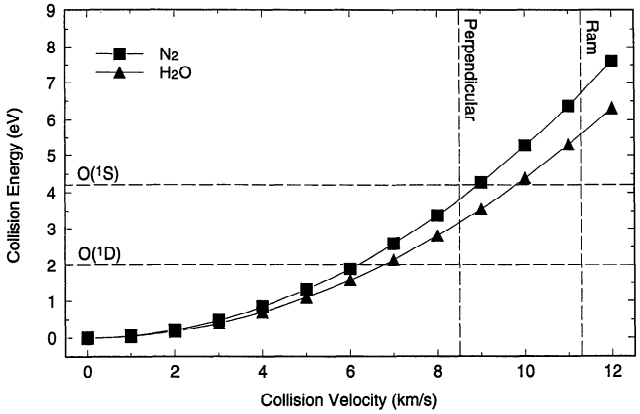

Figure 5. Schematic representation of the energetics of $O(^3P)$ collisional excitation via collisions with H_2O (triangles) and N_2 (squares). The relative velocities of the ram and perpendicular plumes are indicated by the vertical dashed lines. The required excitation energies to achieve the $O(^1S)$ and $O(^1D)$ states are indicated by the two horizontal dashed lines.

consistency information about the analytical approach. For this analysis, we again used the SOCRATES code [*Elgin et al.*, 1990] to calculate the spatial distribution of the emission. A summary of the reaction scheme used is presented in Table 2. In addition to the rate coefficients listed in Table 2 we used the values 150 and 4 s for the lifetimes of the radiative decay processes $O(^1D) \rightarrow O(^3P)$ and $O(^1S) \rightarrow O(^1D)$, respectively. Figure 6 shows two-dimensional plots of $O(^1D)$ and $O(^1S)$ emissions using this scheme. The location of the shuttle is at the intersection of the vertical and horizontal lines and corresponds to the origin of the plots. The plots are such that the minimum intensity shown is about 1/10 of the maximum, and the intensity where the dots merge into solid black is at about 9/10 of the maximum. Further calculations were done for the instrument line of sight, and the agreement between the observations and the calculations is very good. The calculated line-of-sight intensity for the $O(^1S)$ emission was of the order 2×10^9 photons cm^{-2} s^{-1} compared with the 3.5×10^9 photons cm^{-2} s^{-1} from the observations. The uncertainty in the instrument calibration, the thruster parameters, and the atmospheric density used in the SOCRATES model provide more than enough total uncertainty to conclude that the calculations agree with the data. This agreement lends support to the derived rate constant for the second to last reaction in Table 2. Furthermore, an examination of Figure 6 shows the markedly different character of the two emissions. The lower activation energy and the longer radiative lifetime of the $O(^1D)$ state causes the red line emission to be diffusely spread over a large region, whereas the high activation energy and short radiative lifetime of the $O(^1S)$ state causes the green line emission to be more concentrated along the plume axis. Since the present experiment involved a line of sight closely aligned to the plume axis, it substantially enhanced the green line emission in comparison to that seen by a remote observer, such as at the Air Force Maui Optical Site (AMOS) as reported by *Broadfoot et al.* [1992]. With the rate constant derived here the predicted green line emission is approximately 20% as bright as the red line emission for

Table 2. Chemical Reaction Scheme Used in Calculations

Reaction	Preexponential Factor, A	Activation Energy, kJ/mol	Heat of Reaction, kJ/mol
$O(^3P) + N_2 \rightarrow O(^1D) + N_2$	1.28×10^{-11}	190	+190
$O(^3P) + O(^3P) \rightarrow O(^1D) + O(^3P)$	4.44×10^{-12}	190	+190
$O(^3P) + H_2O \rightarrow O(^1D) + H_2O$	1.28×10^{-11}	190	+190
$O(^1D) + N_2 \rightarrow O(^3P) + N_2$	2.30×10^{-11}	0	−190
$O(^1D) + O(^3P) \rightarrow O(^3P) + O(^3P)$	8.00×10^{-12}	0	−190
$O(^1D) + H_2O \rightarrow O(^3P) + H_2O$	2.30×10^{-11}	0	−190
$O(^1D) + H_2O \rightarrow OH + OH$	2.20×10^{-10}	0	−118
$O(^1S) + H_2O \rightarrow O(^1D) + H_2O$	1.50×10^{-10}	0	−215
$O(^1D) + H_2O \rightarrow O(^1S) + H_2O$	3.00×10^{-11}	215	+215
$O(^1S) + O(^3P) \rightarrow O(^3P) + O(^3P)$	2.00×10^{-14}	0	−404
$O(^3P) + O(^3P) \rightarrow O(^1S) + O(^3P)$	2.22×10^{-15}	405	+404
$O(^1S) + H_2O \rightarrow O(^3P) + H_2O$	5.00×10^{-12}	0	−404
$O(^3P) + H_2O \rightarrow O(^1S) + H_2O$	1.50×10^{-13}	405	+404
$O(^1S) + H_2O \rightarrow OH + OH$	3.00×10^{-10}	0	−333

Rate constants are of the Arrhenius form $k = A(T^B)10^{(-EA/kT)}$, where T is the temperature in degrees Kelvin, EA the activation energy in joule per mol, and B is the temperature exponent and is assumed to be 0 in these calculations. The preexponential factor A and the rate coefficient k are in units of cm^3 molecules^{-1} s^{-1}.

the experimental line of sight. However, for a 10 × 10 km region (similar to that viewed by the experiment at AMOS) the total green line emission is calculated to be just 5% as large as the red line emission. This level is consistent with values that would have been difficult to discern in the AMOS data presented by *Broadfoot et al.* [1992].

The temporal nature of the $O(^1D)$ emission is also in agreement with the spectral images in Figures 2a and 2b. The long-lived $O(^1D)$ emission is seen in the spectrum taken immediately after the engine burn. This is consistent with a 150-s lifetime. As mentioned earlier, the 630-nm emission also extends below the shadow line of the OMS pod. The surfaces of the OMS pod are made of white ceramic tiles and are very reflective. The radiating cloud that has blown back over the shuttle (see Figure 6) is reflected off the tiles and creates the appearance that the 630-nm emission extends below the shadow line of the OMS pod.

Conclusion

We report here the first observation of the $(^1S$-$^1D)$ atomic oxygen emission resulting from the firing of the shuttle thrusters into the atmosphere in the ram direction. It is proposed that effluents from the bipropellant, liquid-fueled thrusters collide with the atomic oxygen in the atmosphere to create $O(^1S)$ and $O(^1D)$ states. We have used these observations to calculate an upper limit for the excitation rate coefficient for fast H_2O on O-producing $O(^1S)$. It is noted that the 4.2 eV of energy required for exciting this species is considerable and that the 4.2 eV of energy required for the ^1S state is only available when the thruster is fired into the ram direction. The results of this study are consistent with laboratory measurements of $O(^1S)$ quenching by various collision partners in that only collisions of atmospheric $O(^3P)$ with plume H_2O can adequately account for both the space and ground-based observations of $O(^1S)$ emissions. Further space observations are planned to investigate the velocity dependence by measuring the $O(^1S)$ and $O(^1D)$ emission intensities at a number of intermediate thruster firing directions spanning the wake to ram limits.

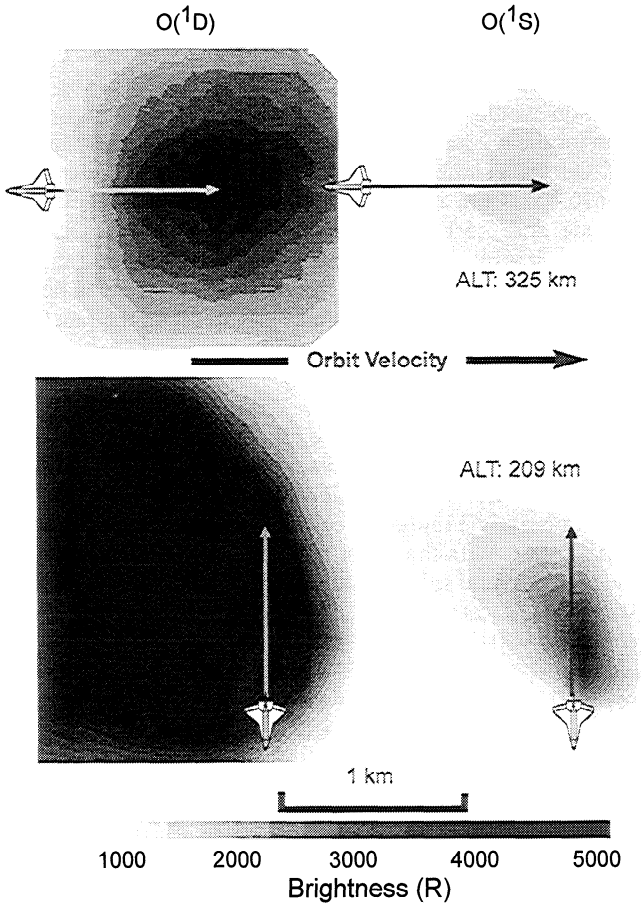

Figure 6. SOCRATES calculations of the spatial maps for $O(^1S) \rightarrow O(^1D) + h$ (λ = 557.7 nm) and $O(^1D) \rightarrow O(^3P) + h$ (λ = 630.0 nm). The shuttle is at the center of each plot and traveling to the right. The thruster was fired into the ram (to the right), and the resulting emissions are indicated as shades of gray representing Rayleighs. The area shown is an 8 × 8 km region around the shuttle, and thus the shuttle is not drawn to scale.

The spatial and temporal distribution of the O(^1S) and O(^1D) emissions is also in agreement with calculations. The O(^1S) emission is more localized, has a shorter lifetime, and appears only while the thruster is fired. The longer-lived O(^1D) emission is observed in the 4-s exposure after the engine has been turned off. The reflection of the 630-nm emission off the OMS pod indicates that the O(^1D) cloud has been blown back over the orbiter by the ramming atmosphere.

Acknowledgments. The Editor thanks B. D. Green and another referee for their assistance in evaluating this paper.

References

Bates, D. R., *Applied Atomic Collision Physics*, vol. 1, *Atmospheric Physics and Chemistry*, edited by H. S. W. Massey and D. R. Bates, pp. 149–223, Academic, San Diego, Calif., 1982.

Broadfoot, A. L., et al., Spectrographic observation at wavelengths near 630 nm of the interaction between the atmosphere and the space shuttle exhaust, *J. Geophys. Res.*, *97*, 19,501–19,508, 1992.

Campbell, I. M., and C. N. Gray, Rate constants for the O(^3P) recombination and association with N(^4S), *Chem. Phys. Lett.*, *8*, 259–273, 1973.

Capetanakis, F. P., F. Sondermann, S. Höser, and F. Stuhl, Temperature dependence of the quenching of O(^1S) by simple inorganic molecules, *J. Chem. Phys.*, *98*, 7883–7887, 1993.

Carignan, G. R., and E. R. Miller, The shuttle induced background: Gaseous constituents, *Adv. Space Res.*, *7(5)*, 153–160, 1987.

Ehlers, H. F. K., Space shuttle orbiter molecular environment induced by the supplemental flash evaporator system, *J. Spacecr. Rockets*, *23*, 379–385, 1986.

Elgin, J. B., D. C. Cooke, M. Tautz, and E. Murad, Modeling of spacecraft contamination, I, Flowfields and methodology of SOCRATES, *J. Geophys. Res.*, *95*, 12,197–12,208, 1990.

Mende, S. B., G. R. Swenson, S. P. Geller, R. A. Viereck, E. Murad, and C. P. Pike, Limb view spectrum of the Earth's airglow, *J. Geophys. Res.*, *98*, 19,117–19,125, 1993.

Pickett, J. S., G. B. Murphy, W. S. Kurth, C. K. Goertz, and S. D. Shawhan, Effects of chemical releases by the STS 3 orbiter on the ionosphere, *J. Geophys. Res.*, *90*, 3487–3497, 1985.

Radzig, A. A., and B. M. Smirnov, *Reference Data on Atoms, Molecules and Ions*, Springer-Verlag, New York, 1985.

Schofield, K., Rate constants for the gaseous interactions of O(2^1D_2) and O(2^1S_0)—Critical evaluation, *J. Photochem.*, *9*, 55–68, 1978.

Scialdone, J. J., An estimate of outgassing of space payloads and its gaseous influence on the environment, *J. Spacecr. Rockets*, *23*, 373–378, 1986.

Slanger, T. G., and G. Black, O(^1S) interactions—The product channels, *J. Chem. Phys.*, *68*, 989–997, 1978.

Trinks, H., and R. J. Hoffman, Experimental investigation of bipropellant exhaust plume flowfield, heating, and contamination and comparison with the CONTAM computer model predictions, in *Spacecraft Contamination: Sources and Prevention*, edited by J. A. Roux and T. D. McCay, pp. 261–273, American Institute of Aeronautics and Astronautics, New York, 1984.

Viereck, R. A., E. Murad, B. D. Green, P. Joshi, C. P. Pike, R. Heib, and G. Harbaugh, Origin of the shuttle glow, *Nature*, *354*, 48–50, 1991.

Viereck, R. A., S. B. Mende, E. Murad, G. R. Swenson, C. P. Pike, F. L. Culbertson, and R. C. Springer, Spectral characteristics of shuttle glow, *Geophys. Res. Lett.*, *19*, 1219–1222, 1992.

Viereck, R. A., L. A. Bernstein, S. B. Mende, E. Murad, G. R. Swenson, and C. P. Pike, Visible spectra of thruster plumes from the space shuttle primary reaction control system, *J. Spacecr. Rockets*, *30*, 724–730, 1993.

Wulf, E., and U. von Zahn, The shuttle environment: Effects of thruster firings on gas density and composition in the payload bay, *J. Geophys. Res.*, *91*, 3270–3278, 1986.

L. S. Bernstein and J. B. Elgin, Spectral Sciences Inc., Woburn, MA 01803.

S. Lucid, Astronaut Office NASA Johnson Space Center, Houston, TX 77058.

S. B. Mende and G. A. Swenson, Lockheed Research Division, 3251 Hanover St., Palo Alto, CA 94304.

E. Murad, C. P. Pike, and R. A. Viereck, Phillips Laboratory, Spacecraft Interactions Branch, 29 Randolph Rd., Hanscom AFB, MA 01731-3010. (e-mail: viereck@plh.af.mil)

(Received November 2, 1993; revised December 19, 1994; accepted December 19, 1994.)